Molecular Dynamics Simulation of the Cytosolic Mouth in Kcv-Type Potassium Channels†

Sascha Tayefeh,‡,§ Thomas Kloss,‡ Gerhard Thiel,§ Brigitte Hertel,§ Anna Moroni,|| and Stefan M. Kast*,‡

Eduard-Zintl-Institut für Anorganische und Physikalische Chemie, Technische Universität Darmstadt, Petersenstrasse 20, 64287 Darmstadt, Germany, Institut für Botanik, Technische Universität Darmstadt, Schnittspahnstrasse 3, 64287 Darmstadt, Germany, and Dipartimento di Biologia, CNR-IBF and INFM, Consiglio Nazionale della Ricerche-Istituto di Biofisica e Istituto Nazionale Fisica della Material, Unità di Milano Università, Via Celoria 26, 20133 Milan, Italy

Received November 30, 2006; Revised Manuscript Received February 13, 2007

ABSTRACT: The functional effect of mutations near the intracellular mouth of the short viral Kcv potassium channel was studied by molecular dynamics simulations. As a model system we used the analogously mutated and truncated KirBac1.1, a channel with known crystal structure that shares genuine local sequence motifs with Kcv. By a novel simulated annealing methodology for structural averaging, information about the structure and dynamics of the intracellular mouth was extracted and complemented by Poisson−Boltzmann and 3D-RISM (reference interaction site model) integral equation theory for the determination of the K^+ free energy surface. Besides the wild-type analogue of Kcv with its experimental reference activity (truncated KirBac1.1), two variants were studied: a deletion mutant where the N-terminus is further truncated by eight amino acids, showing inactivity in the Kcv reference system, and a point mutant where the kink-forming proline at position 13 is substituted by alanine, resulting in hyperactivity. The computations reveal that the change of activity is closely related to a hydrophilic intracellular constriction formed by the C-terminal residues of the monomers. Hyperactivity of the point mutant is correlated with both sterical and electrostatic factors, while inactivity of the deletion mutant is related to a loss of specific salt bridge patterns between the C- and N-terminus at the constriction and to the consequences for ion passage barriers, as revealed by integral equation theory. The cytosolic gate, however, is probably formed by the N-terminal segment up to the proline kink and not by the constriction. The results are compared with design principles found for other channels.

Kcv, a viral potassium channel from the *Paramecium bursaria* chlorella virus (PBCV-1),[1] represents the shortest sequence of a functional channel known to date (*1*). As a minimal working model this K^+ channel protein can be considered close to being prototypical in order to understand basic channel design principles and to gain insight into fundamental transport mechanisms (*2*, *3*). With a monomer length of only 94 amino acids this protein comprises basically just the pore region of all K^+ channels. Kcv exhibits high topological similarity with other channels, including the selectivity filter signature sequence TXXTXGY/FG (*4*), a pore helix, and two transmembrane domains (TM1/TM2). These most likely correspond to outer domain TM1 and inner, cavity-forming domain TM2. Kcv is characterized by a short C-terminal TM2 inner helix and the absence of downstream cytosolic domains as well as an extraordinarily short N-terminus upstream of TM1. Homology modeling based on the crystal structure of the bacterial KirBac1.1 channel (*5*) indicates that the N-terminal part is equivalent to the "slide" helix. In both channels this domain is connected with a kink-forming proline to TM1 (*6*).

Despite the short sequence Kcv shares many functional characteristics with longer channels, including sensitivity to common K^+ channel blockers and the ability to exhibit voltage-dependent gating. The question therefore arises as to the location and function of the gate(s) in the Kcv system in comparison with other K^+ channels. This will allow insight into the generality of gating mechanisms. Currently, there is evidence for two gates in K^+ channels: many experimental and computational studies on channels with known crystal structures support the presence of a hydrophobic gate at the tight cytoplasmic constriction formed by the TM2 helix bundles (see, e.g., refs *7*−*14*). There is also strong evidence for the selectivity filter directly acting as a gate (*14*−*17*). The situation is most likely far more complex as suggested

† This work was supported in part by the Deutsche Forschungsgemeinschaft (to G.T. and S.M.K.), Fonds der Chemischen Industrie and the Adolf-Messer-Stiftung (to S.M.K.), and the Ministero Istruzione Università e Ricerca, Progetto Fondo per gli Investimenti della Ricerca di Base (to A.M.).

* To whom correspondence should be addressed. E-mail: kast@pc.chemie.tu-darmstadt.de. Tel: +49 (6151) 165397. Fax: +49 (6151) 164298.

‡ Eduard Zintl-Institut.

§ Institut für Botanik.

|| Dipartimento di Biologia.

[1] Abbreviations: PBCV-1, *Paramecium bursaria* chlorella virus; TM1/TM2, transmembrane domains; WT, wild type; KB-KcvWT/KB-KcvP13A/KB-KcvΔN8, KirBac1.1-Kcv chimera mutants; MD, molecular dynamics; PB, Poisson−Boltzmann; RISM, reference interaction site model; PDB, Protein Data Bank; TIP3P, three-point transferable interaction potential; NpT, constant particle number, pressure, and temperature; GFP, green fluorescent protein; DMPC, dimyristoylphosphatidylcholine; RMSD/F, root mean square deviation/fluctuation; MDIIS modified direct inversion of iterative subspace; KH, Kovalenko−Hirata.

10.1021/bi602468r CCC: $37.00
Published on Web 03/31/2007

by the presence of couplings between the intracellular and extracellular gates (*18*): there is evidence as to the existence of open yet inactive pore states involving both gates. In contrast, recent computational work using elastic network models does not reveal such coupling (*19*). Instead, local concerted motion of both transmembrane segments associated with inner gate opening/closing transitions is apparently uncorrelated with the selectivity filter dynamics. This is found as a common scheme among known K^+ channel structures. It is, however, questionable whether a purely harmonic network model would reveal such a cooperative behavior.

In this context, a further interesting feature of the small Kcv structure is that channel gating is influenced by structural elements far away from either the potential selectivity filter gate or the cytoplasmic end of TM2. A comparison of Kcv with orthologues from other chlorovirus isolates has shown that an amino acid exchange in the outer transmembrane domain (TM1) is sufficient to inverse the voltage dependence of the channel; a mutation V19F within TM1 of the Kcv channel from virus MA-1D shifts the channel from a mild inward rectifier into an outward rectifier (*6*). These features cannot be explained on the basis of structural features alone.

Although the C-termini in Kcv are presumably too short to exhibit bundle crossing as a signature for the inner gate found in other channels, the cytosolic side adjacent to the intracellular mouth is yet involved in Kcv gating. This has been demonstrated by electrophysiological experiments on mutants: replacing Pro13 by alanine (KcvP13A) in the N-terminus yields a hyperactive channel, which is characterized by a gain of a time- and voltage-dependent component (*20*). A possible explanation considers that the increased hydrophobic length of TM1 in KcvP13A leads to a change of helix orientation in the lipid environment which, as a consequence, could affect gating. Complete truncation of the "slide helix" in Kcv results in channel inactivation (*21*). Progressive truncation of the N-terminus revealed that inactivation occurs if nine or more amino acids are removed (KcvΔN9). Very weak activity is found for KcvΔN8, whereas longer slide helices preserve channel functionality (*22*). In the context of the aforementioned model on the orientation of TM1 the latter data were interpreted in such a way that the cytoplasmic N-terminus requires a sufficient length for anchoring and positioning of TM1 in the membrane. This hypothesis requires further microscopic scrutiny.

Insight into structural, thermodynamic, and dynamical features of the intracellular mouth region of Kcv wild type and mutants on the atomic level would therefore mean a major step forward in testing current hypotheses of mechanistic generality of gating transitions in K^+ channels. The crystal structure of Kcv is, however, not known until now, so all structure−function relationships established so far were based on multiple alignment and homology models. In this work, we used molecular dynamics (MD) simulations of model channels in a fully solvated lipid environment as a basic tool for generating structural and dynamical data in order to understand the wild-type structure of Kcv and the effects of mutations. Atomistic MD simulation is a well-established computational tool in the area of potassium channel studies (see, e.g., refs *10*, *11*, *14*, and *23*−*28*). These are typically based upon the experimental crystal structures of the target proteins, although many examples of successful simulations of homology models have been described in the literature (see, e.g., refs *29*−*32*). As an alternative, one can directly study analogous model systems with known crystal structures that share essential sequence motifs with the target protein. In this case the simulation will be more stable and the resulting ensemble averages more reliable; the results are to a lesser degree confounded by uncertainties about the underlying structure as compared to pure homology models. The results can be interpreted under the hypothesis of functional analogy between model and target systems. Since the sequence similarity of Kcv with other structurally known channels is quite low, we decided to proceed with such an approach at the present stage: the KirBac1.1 structure was truncated to match the shorter Kcv protein variants described above. KirBac1.1 was chosen because it contains the pivotal proline residue forming the onset of the slide helix in analogy with Kcv. Furthermore, mutations were inserted at equivalent positions to mimic the experimental alterations in Kcv. The resulting chimeras are termed KB-KcvWT, KB-KcvP13A, and KB-KcvΔN8. KB-KcvΔN8 shares with the totally inactive KcvΔN9 the feature that all positively charged amino acids in the N-terminus (arginine in Kcv vs the corresponding lysine in KirBac1.1) are deleted, which will be of special importance.

In addition to the biological questions we were particularly interested in the application of methods commonly employed in structural biology to our simulation results. These include interpretation of local structural features, motifs, and sterical permeation constraints as well as the use of Poisson−Boltzmann (PB) theory for characterizing the electrostatic ion passage free energy surface (*33*). To this end a substantial part of the present work was devoted to the development of a novel annealing procedure for extracting average all-atom structures from very long trajectories. The tetrameric symmetry is fully taken into account, making it possible to present the results of extensive MD simulations of the three model systems in a very compact way.

Furthermore, integral equation theory in the form of the three-dimensional reference interaction site model (3D-RISM) (*34*, *35*) was applied to the symmetrized structures, yielding insight into potassium density distributions around the tetrameric channels and into its spatial dependence on the mutation state. Large density at a given point in space is directly related to negative values of the potential of mean force accompanying single-ion transport from the bulk to this region in the mean field of the environment. In the past, the site-averaging 1D-RISM theory has been applied to small fragments of the KcsA filter region (*36*, *37*). To the best of our knowledge, this is the first time that 3D-RISM theory has been used for characterizing the ion free energy surface of a full-size potassium-selective channel.

METHODS

Modeling Wild Type and Mutants. Among the available X-ray structures of K^+ channels [KcsA (*38*), MthK (*39*), KvAP (*40*), KirBac1.1 (*5*), Kv1.2 (*41*), and, discovered only after we started with the present work, NaK (*42*)] we chose KirBac1.1 (PDB code 1P7B) as the prototype system for building Kcv-analogue channel models because of the pivotal proline position that marks the start of the KirBac1.1 slide helix corresponding to Pro13 in Kcv. Sequence alignment in order to localize a suitable C-terminal truncation of the

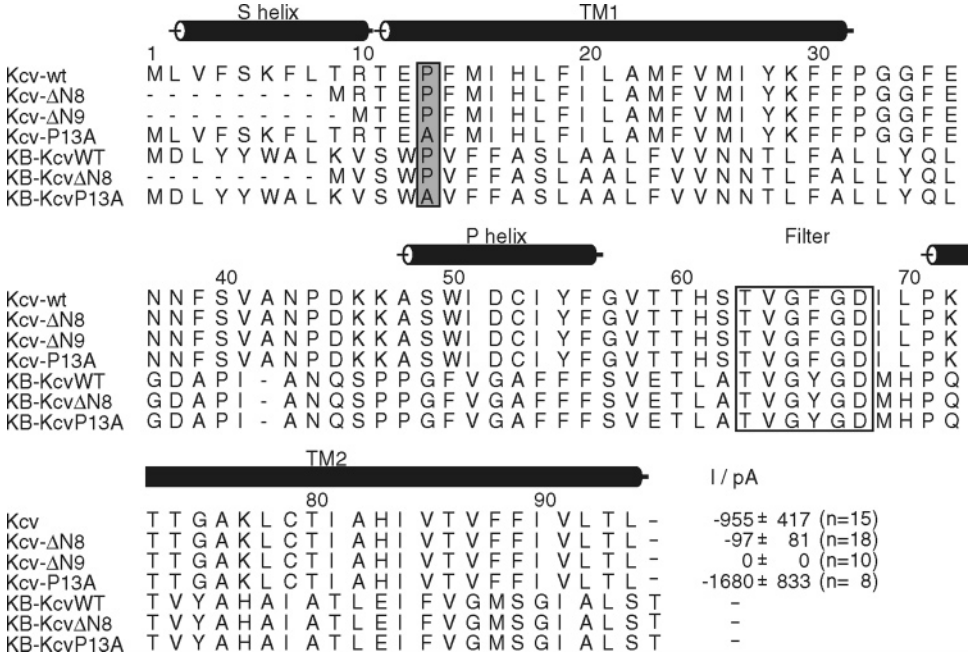

FIGURE 1: Sequence and secondary structure of KcvWT and mutants with their KirBac1.1 analogues. The filter and the position of Pro13 are marked by boxes (abbreviations: s = slide, p = pore, TM = transmembrane domain). The mean steady-state currents of HEK293 cells expressing a chimera of KcvWT or mutant channels were measured as in ref *6* at −160 mV; the currents exceeding the mean current of mock-transfected cells are given (*20*, *22*).

KirBac1.1 sequence has been performed along the lines of our earlier work (*6*), taking into account the suggestion given in ref *43*. The final alignment is shown in Figure 1.

Atomic models of wild-type (KB-KcvWT) and deletion mutant (KB-KcvΔN8) chimeras were produced with the academic version of CHARMM V3b1 (*44*). For KB-KcvWT and KB-KcvΔN8 residues 1−49 and 1−57, respectively, as well as residues 142−309, were removed, leaving proteins of 94 and 86 amino acids per subunit. In all cases the resulting N-terminal residue was mutated into methionine. For the point mutant analogue (KB-KcvP13A), the expected change of local fold geometry due to replacing the kink-forming proline by alanine was taken into account by using Modeller V8.1 (*45*) in order to anneal into an optimal structure. The optimization in the field of knowledge-based potential derived from crystal structure statistics satisfies additionally spatial restraints of the template structure KB-KcvWT. In order to prevent both distortion of the sensitive filter region and displacement of the K^+ ions provided by the crystal structure, those positions were rigidly constrained during the annealing process.

Finally, hydrogen atoms were attached using CHARMM's "HBUILD" facility, followed by all-atom energy minimization by steepest descent and Newton−Raphson methods. The wild-type analogue coordinates were shifted with respect to the center of mass; the mutants were superimposed onto this structure in order to maintain comparable conditions for subsequent membrane insertion. Titratable residues were kept at their standard protonation state. The C-terminal threonines were deprotonated; the N-terminal methionines were protonated. Some discussion in the literature concerns the protonation state of Glu106 in KirBac1.1 that corresponds to Glu71 in KcsA and Glu58 in our wild-type chimera (*16*, *46*). In our model we decided not to bias the simulation toward a specific template K^+ channel structure, so glutamate was kept in its deprotonated standard state during simulations. We have checked the influence of the protonation state on the electrostatic free energy surface in the central cavity (see below).

Molecular Dynamics Simulations. All simulations were performed with the NAMD 2.5 molecular dynamics program (*47*) using all-atom potential energy functions CHARMM22 for proteins (*48*) and CHARMM27 for phospholipids (*49*). The TIP3P water model (*50*) and KCl as electrolyte were used. Lennard-Jones parameters of the ions were $\epsilon = 0.087/0.15$ kcal mol^{-1} and $R_{min}/2 = 1.76375/2.27$ Å for K^+/Cl^- (*51*). Bonds between heavy atoms and hydrogen were kept fixed using the SHAKE algorithm (*52*). Throughout, a time step of 2 fs was applied, Lennard-Jones interactions were switched smoothly to zero over a distance between 10 and 12 Å, and electrostatics were treated by the particle mesh Ewald algorithm (*53*) with a Fourier grid of 72 × 72 × 96 points corresponding to ca. 1 Å resolution. Constant temperature conditions were realized at 330 K by a Langevin thermostat (coupling constant 5 ps^{-1}, not applied to hydrogen); constant pressure was set to 1 atm by applying the Langevin piston algorithm (*54*, *55*) with an oscillation period of 200 fs and damping time scale of 100 fs.

The complete simulation system composed of tetrameric protein, lipid, and aqueous KCl solution was assembled following closely the protocol developed and provided by Roux and co-workers (*24*, *51*, *56*). In short, first, a protein−membrane system is built and minimized using a set of preequilibrated lipid molecules, and in parallel a water box is equilibrated; second, the two subsystems are merged, minimized, and preequilibrated followed by insertion of ions satisfying a given average concentration and overall charge neutrality.

In our special case the distance between the terminal residues of the longest transmembrane domain TM1 along the *z*-axis (the membrane normal) is around 34 Å. Thus DMPC has been chosen to build the bilayer since the

thickness of a DMPC bilayer is of similar dimensions. For every model the cross-sectional area in the *xy* plane was calculated. The maximum area occupied by the protein models was determined for either of the monolayers and subtracted from the box area. According to the discussion in ref *24*, a cross-sectional area of 59 $Å^2$ per DMPC molecule was assumed to be a reasonable value. The approximate number of lipid molecules required for either side was calculated. This number was used as a starting point and adapted where necessary to the specific needs of every system. Several values were tested in a number of attempts by short MD runs. Using too many lipid molecules stalls the building procedure whereas too few lipids would allow too many water molecules to penetrate the membrane. Stable results were obtained for 62/68/69 DMPC molecules on the intracellular side and 54 throughout on the extracellular side for KB-KcvWT/KB-KcvΔN8/KB-KcvP13A, respectively. The total number of atoms was 48561/48869/49026 at a concentration of ca. 100 mM KCl. Thus, all systems contained 33 potassium ions, 17 chloride ions, and 9701/9765/9586 water molecules, respectively. The initial dimensions of the orthorhombic simulation cell were 92 Å along the *z*-axis and 72 Å along in the *xy* plane.

In addition to the harmonic restraints that were gradually removed during the building procedure, we applied strong restraints (force constant 10 kcal mol^{-1} $Å^{-2}$) to the filter residues (TVGYGD) and to the K^+ ions in the filter to prevent distortion of this sensitive region during all of the equilibration and most of the production time. Only at the end of the construction, a very short restraint-free NpT run of 20 ps was performed in order to allow the filter region to accommodate before rerestraining. According to the electrolyte concentration we have placed two restrained K^+ ions on binding positions S1 and S3 using the terminology defined in ref *26* and two restrained water molecules on S0 and S2 in the filter. In total, trajectories of 45 ns were produced for each model. Filter restraints were applied during the first 30 ns and lifted for the remaining 15 ns in order to probe stability. For the structural averaging procedure to be described below only the last 21 ns of the rigid filter runs was used. Trajectory data were stored every 1 ps.

Symmetrizing Structural Averaging by Simulated Annealing. One of our main goals for assessing differences between wild type and mutants was to condense the information of very long trajectories into meaningful all-atom average structures. Simple averages are unsuitable over longer times since, for instance, rotatable groups could collapse into single sites and cause a loss of backbone integrity. The key idea realized in this work was to use average distances measured over the trajectories as target values for a simulated annealing procedure on the isolated tetramer. This is equivalent to minimization in the mean field of the environment that is effectively encoded by the harmonic restraint distances. Rotational symmetry can additionally be imposed during annealing in order to allow for subsequent analysis of simulation data by computational means that have been applied in the past to crystal structures only.

The procedure is summarized as follows: (i) Heavy atom distances are averaged over the production run, taking into account topologically equivalent sites within the subunits. Intersubunit distances are calculated and averaged separately for neighboring and opposite pairs. (ii) For defining restraints, all Cα pair distances are considered; for all other heavy atom pairs only those within a target cutoff distance of 11 Å are taken into account. (iii) Restraint force constants of 10 kcal mol^{-1} $Å^{-2}$ between Cα−Cα pairs and of 0.1 kcal mol^{-1} $Å^{-2}$ for all others are assigned, weighted by the inverse fluctuation of the target distances measured in angstroms. (iv) Starting with the crystal structure-like initial models of the chimeras, the isolated tetrameric proteins are optimized first within the CHARMM force field augmented by the restraints (including heavy filter restraints with a force constant of 1000 kcal mol^{-1} $Å^{-2}$) by 100 steps of steepest descent and 50 steps of adopted-basis Newton−Raphson minimization. (v) The global minimum of the model is approached by a symmetrizing simulated annealing procedure using Langevin dynamics with a friction constant of 10 ps^{-1} and a time step of 1 fs within CHARMM.

The latter part is defined by a temperature schedule comprising the following steps: (va) starting with the temperature T_0, T is kept constant over a period Δt. (vb) T is quenched linearly to $T_1 = T_0 - 200$ K over Δt. (vc) T is kept constant at T_1 over Δt, followed by symmetrization. (vd) T is increased instantaneously to $T_2 = T_1 + 100$ K. Steps va−vd are repeated by setting $T_0 = T_2$ and increasing Δt by a factor of 1.1 until a target temperature of 0 K or below is reached. In this case a final MD minimization at 0 K over Δt is performed. After step vc in each cycle, symmetrization is achieved by first computing average structures over the last constant temperature window and superposition of three monomers onto one with respect to filter atoms and heteroatoms, followed by averaging all topologically equivalent atoms and resuperposition of the resulting average monomer structure onto the original asymmetric tetramer of this cycle step.

Beside other parameters we have optimized independently and then kept fixed, two quantities influence the performance of the annealing protocol: initial temperature T_0 and interval Δt. We have tried a variety of combinations in the range 250−1500 K and 200−1000 fs. Best results in terms of minimal RMS (root mean square) deviations (RMSD) between target and optimized distances measured for the final models were obtained with $T_0 = 750$ K and $\Delta t = 200$ fs. This parameter set leads to total RMSDs of 0.458/0.423/0.587 Å for all restraint distances in KB-KcvWT/KB-KcvΔN8/KB-KcvP13A, respectively, and was used throughout in the following. The RMSD of all Cα pairs in the rigid filter simulation of wild type and mutants is additionally depicted in the top part of Figure 2, emphasizing the performance of the approach.

Structural and Thermodynamic Evaluation. Besides standard techniques for evaluating simulation results like the computation of RMS fluctuations (RMSF) and RMS deviations of the structures as they evolve from the initial state, we also used HOLE analysis (*57*) for analyzing the pore diameter and Poisson−Boltzmann theory (*58*) for accessing the electrostatic free energy surface of K^+ entering the channel from the bulk solution, as well as 3D-RISM integral equation theory (*34*, *35*) for a realistic view on potassium density distributions. The RMSD calculations were carried out with the RMSDTT v1.9.2.2 plugin (*59*) for VMD v1.8.3 (*60*). HOLE, PB, and 3D-RISM analyses were applied to the symmetrized average structures. Averaging procedures like the one described above are dangerous if gating events

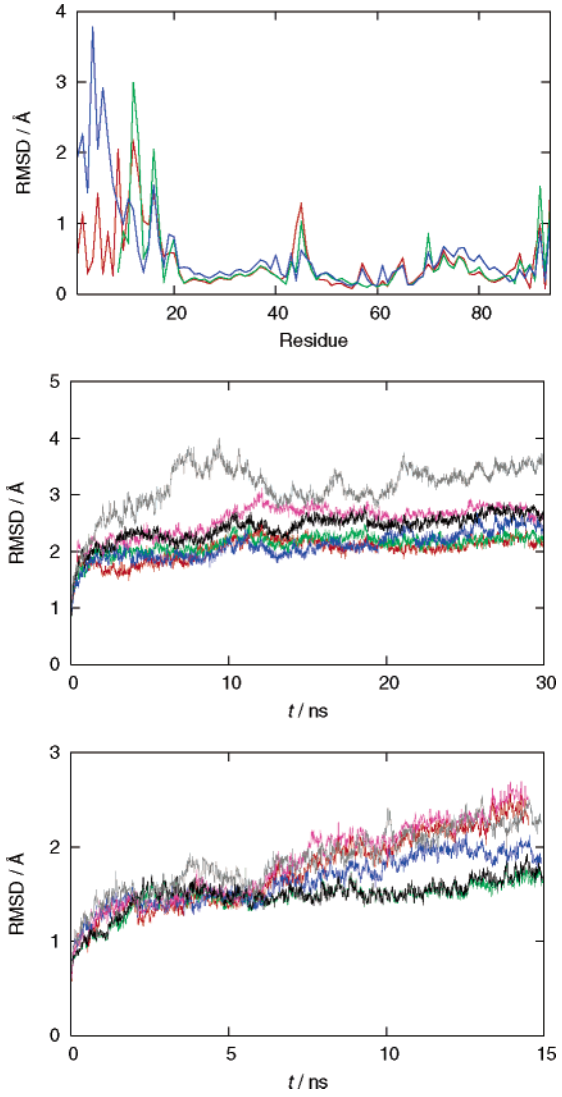

FIGURE 2: RMS deviation between globally optimized and target backbone Cα pair distances obtained from the symmetrizing simulated annealing procedure (top). Backbone RMSD time series of the structures: rigid filter runs (middle) and subsequent fully relaxed simulations (bottom; time was reset to zero). Color code: red/magenta (excluding N-terminus/full protein), KB-KcvWT; black/green, KB-KcvΔN8; gray/blue, KB-KcvP13A.

in the form of global conformational changes had occurred during the simulation time scale. These are inaccessible to unbiased MD simulation with present-day resources and did not happen in our models. As we will show below, our simulation model corresponds to the open state of the channel, warranting the evaluation of averaged structures.

When interpreting purely structural information one must, however, not overinterpret rigid structure results since sterical barriers may disappear easily due to short-scale dynamics (*33*). In contrast, electrostatic fields are of wider range, vary less steeply, and are less sensitive to short-scale dynamics. Both measures together yield a sensible picture of barriers and (de)stabilizing forces accompanying ion transport between bulk solvent and the channel pore. The integral equation approach covers basically both components within a single methodology. Though the theory is approximate, the underlying molecular models of solute (the channel) and solvent (aqueous KCl solution) are identical with those used in the simulations. In this way, we are able to characterize the scenario in a much more realistic way, beyond the capabilities of more simplified HOLE and PB approaches, but with comparable computational effort.

Our PB treatment for a given channel geometry follows closely the procedures outlined earlier by Roux and coworkers (*33*) (particularly ref *61*). As a result we obtain the electrostatic free energy change accompanying K^+ transport from the bulk to a point in the pore along the reaction coordinate defined to be the *z*-axis connecting the filter ions and the center of the cavity which is set to $z = 0$. The membrane is described as a planar slab with a height of 25 Å. The interior of the protein is confined by the van der Waals radii of its atoms (*62*) using a probe radius of 1.4 Å. A cylinder with radius 12 Å representing the solvent-filled pore was cut out from the membrane slab. The relative dielectric constant of the aqueous solution and the cylinder was set to 80 whereas a value of 2 was assigned to the hydrocarbon core of the membrane as well as to the protein interior. PB calculations with the built-in PBEQ module (*63*) of CHARMM were performed in two stages, first with a cubic grid of 140^3 points and an initial grid spacing of 1 Å and afterward focusing around the main region with half of the grid spacing. Periodic boundary conditions were applied in the membrane *xy* plane. The two K^+ ions in the filter were kept fixed while a third K^+ was placed in intervals of 0.5 Å along the reaction coordinate for computing the transfer free energy under varying ionic strength conditions.

The solution to 3D-RISM theory requires two steps: first, the determination of the pure solvent susceptibility, and second, the computation of the 3D density distribution of the respective solvent around the channel. In this second stage the fully solvated tetrameric protein only was taken into account, excluding the membrane. The KCl/TIP3P susceptibility was determined by solving the dielectrically consistent 1D-RISM equations (*64*, *65*) on a logarithmically spaced grid of 512 points ranging from 5.98×10^{-3} Å to 164.02 Å using a variant of the modified inversion of iterative subspace (MDIIS) method (*66*). Small Lennard-Jones parameters ($\sigma_H = 0.4$ Å, $\epsilon_H = 0.046$ kcal mol^{-1}) were attributed to the hydrogen sites of TIP3P in order to avoid numerical singularities. Temperature was set to 298.15 K and electrolyte concentration to 1 M corresponding to number densities for water of 0.032367 Å^{-1} and for KCl of 0.000602 Å^{-1} (*67*). The relative dielectric constant of the solvent was taken as 68.5 (*68*). The 3D-RISM equations were solved within the partially linearized Kovalenko−Hirata (KH) closure approximation (*69*) on a cubic grid of $128 \times 128 \times 128$ points with a 0.6 Å spacing by the MDIIS technique (*66*). Long-range electrostatics were treated by Ewald summation (*69*), taking into account conducting boundary conditions. No fixed potassium sites were present; the protonation states of the proteins were identical with the MD simulation models. All integral equation computations were performed using a computer code developed in our laboratory. The density distributions were visualized by the MOLCAD program (*70*).

RESULTS

Phenomenology of the Simulations. Besides monitoring total energy, density profiles, etc., which all indicated progress toward equilibrium which is practically reached with respect to these observables after a few nanosecoonds, we

report here only results of the backbone RMSD as a measure of structural drift from the initial models (see Figure 2, middle and bottom parts). While the simulations with rigid filter restraints ("rigid filter simulations") appear to be fairly stable, relaxing the filter has a strong effect, as expected (*16*, *71*): ions move rapidly into another configuration, from S1/S3 to S2/S3 in the terminology defined in ref *26*, which in turn leads to substantial filter distortion; this progressively extends to other regions of the protein. We consequently used for long-time structural averaging only the rigid filter runs. This is justified because of the apparent low mobility of the filter and the locality of associated transitions (*19*, *72*). By dissecting the RMSD further into the N-terminal slide helix and into other regions' contributions, it becomes clear that particularly the N-terminus undergoes larger amplitude motion, as shown in Figure 2, middle and bottom: While the RMSD time series appears to be reasonably stable for the backbone atoms excluding the slide helix, somewhat stronger deviations are observed for the full sequence. The flexibility is also reflected in Figure 2, top, in terms of the RMSD values obtained for the symmetrized structures, which are largest in the N-terminal part.

Simple structural averages over the last 7.6 ns of the rigid filter simulations are shown in the upper left part of Figure 3. The most relevant structural features are the following:

(a) It is evident from the comparative structures that the P13A mutant has a TM1 segment which is much more flexible than in the two other channels. This leads to an increased asymmetry among the monomers within the tetramer. The effect of the mutation on TM1 flexibility is, however, rather local and mostly confined to the inner mouth of the channel. All models agree structurally quite well for any region except the slide helices. The same statement holds for the fully relaxed simulation results, so we do not suffer from artifacts related to the rigid filter geometry.

(b) The slide helix attached to TM1 does not exhibit significant contact with the surrounding membrane headgroups. This is in marked contrast to recent computational results concerning the KirBac1.1 gating mechanism (*73*) where it was shown that varying contact patterns between aromatic residues in the slide helix and the lipid phase accompany the gating transition.

(c) In line with our earlier results (*6*), TM2 is too short to exhibit bundle crossing in order to realize the canonical closed state of the channel. Furthermore, in contrast to earlier observations concerning the gating mechanisms of known channel structures (*11*), we cannot identify any significant change of TM2 upon mutation or during the simulations. This suggests that the measured stochastic opening and closing (*74*) as well as the differences in channel activity between WT and mutant Kcv channels are not caused by motion of the inner TM domain.

(d) The simulations revealed the presence of four stable intramonomer K^+ binding sites, located between Glu58 and Asp67 in each monomer (numbering according to Figure 1; note the alignment gap in the KirBac1.1 sequence near position 41). This complements the discussion about the protonation state of the respective glutamate (see above in subsection Modeling Wild Type and Mutants) since apparently a positive charge (being either a proton or a K^+ ion) is required at this position.

While the structural observations already suggest that the cytosolic side of the pore is open, we also have dynamical support for this view. We have observed spontaneous ion transitions from the bulk into the central cavity, although we constructed the cavity initially to be ion-free. To the best of our knowledge this is the first observation of this kind of dynamics (see Figure 4). Over the whole of the trajectories (constrained and unconstrained), KB-KcvWT behaves markedly different as compared to the mutants: almost immediately after the start of the simulations a first K^+ ion entered the cavity and stayed at a position close to the filter. Other ions frequently entered and exited; on average, two ions occupied the cavity. Ion transport through the intracellular mouth is accompanied by coordination and subsequent release by the C-terminal carboxyl groups. In the case of the P13A mutant the cavity appears to be less favorable for cation stabilization: only after the filter restraints had been lifted, a single ion moved into the cavity. For KB-KcvΔN8 we observed a similar stabilization for the first ion that passed the mouth and immediately moved close to the filter. A second one, however, got expelled after some time, whereas another cation got basically trapped between the C-terminal carboxyl groups by tight coordination after 300 ps simulation time. This state remained stable over the rest of the trajectory, blocking further ion entrance or exit. We have therefore the first indication that the deletion mutant forms an open yet inactive pore state. Later on we will show that all dynamical features that have been observed correspond well with thermodynamic and structural observables in order to explain the differences in conductivity.

Symmetrized Average Structures. A more detailed picture of the effects of the mutations on structure−function correlates is obtained by analyzing the symmetrized average structures from the simulated annealing procedure. Figure 3 depicts in the upper right part the superposition of the resulting structures of the three variants onto each other and in the lower part the geometries together with color-coded local backbone atomic *B* factors computed over the final 4.5 ns of rigid filter production runs, and accessible free volume from HOLE analysis. In this representation the effect of the P13A mutation becomes more clearly visible: there is a tendency toward helix elongation of TM1 caused by removing the kink-forming proline; this is in line with earlier results (*6*). But unlike speculated earlier (*6*) this helix elongation does not lead to more pronounced helix/membrane contacts; the orientation of TM1 in the membrane is not significantly affected. Overall, we see confirmation for the highly localized effect of the mutations at the inner part of the protein. The increased N-terminal flexibility has a counterpart in the corresponding C-termini in KB-KcvP13A. Quite evidently, the inner constriction (defined as the smallest diameter found by HOLE analysis) is substantially enlarged in KB-KcvP13A; in contrast, the wild type and deletion mutant show only insignificant differences.

An interesting result of the present data is that TM2, despite of its short length, forms a constriction by the C-terminal amino acids. The diameter can become very small, comparable with the size of the K^+ ion. The estimated size of the inner constriction suggests that it could obstruct passage of ions. Nonetheless, the open character of the inner mouth and the local flexibility of TM2 preclude the assumption that this hydrophilic constriction is identical with the

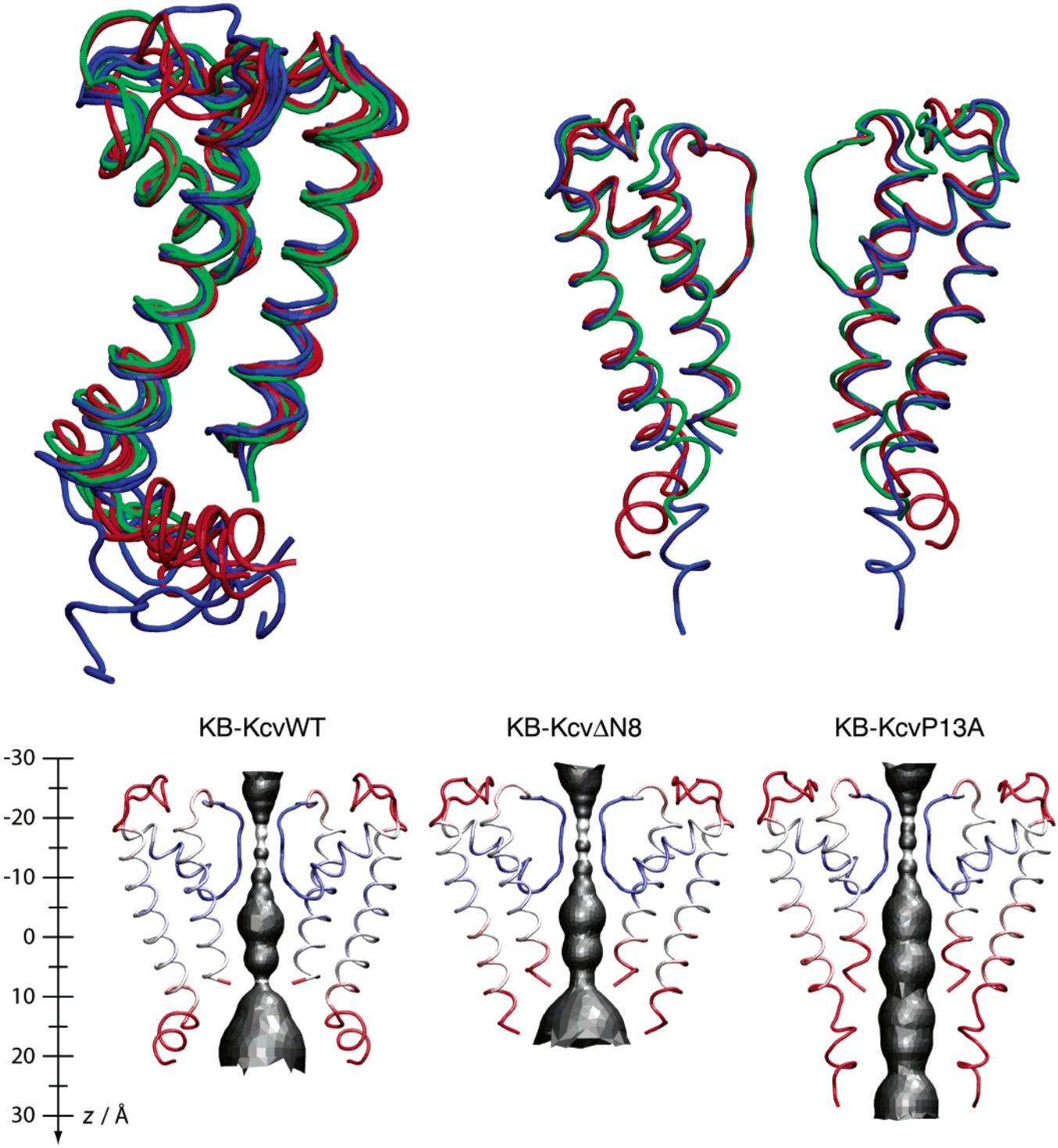

FIGURE 3: Superposed backbone structures from simple averaging over the final 7.6 ns of the rigid filter runs (top, left). Superposition of structures from the symmetrizing simulated annealing procedure (top, right; only two subunits are shown for clarity): red, KB-KcvWT; green, KB-KcvΔN8; blue, KB-KcvP13A. HOLE analysis and backbone atomic *B* factors (blue, <10 Å^2; red, >20 Å^2) mapped onto symmetrized structures (bottom).

inner gate in this channel.

The global situation around the N-terminal constriction becomes clearer when we take results from Poisson−Boltzmann theory into account. Figure 5 shows free energy data for the three variants with two different protonation states of Glu58. Also included are the curves for the initial wild-type model (a truncated KirBac1.1 pore) before simulation as well as for the native KirBac1.1 geometry from X-ray crystallography, both for an ionic strength of 0 and 100 mM. Comparison of native and truncated KirBac1.1 reveals that mere truncation already has a drastic effect on the free energy surface, making the cavity overall favorable for cation binding. Accordingly, the electrostatic barriers to K^+ entry from the cytosol are very small for all of our chimeras, indicating again the open state for any variant under scrutiny. In line with findings for other channels (*61*), less favorable transfer free energy within the cavity corresponds to a higher conductance state. This is indeed consistent with our findings for KB-KcvP13A: the barrier to inward current (i.e., from the cavity into the cytosol) in the mutant decreases in

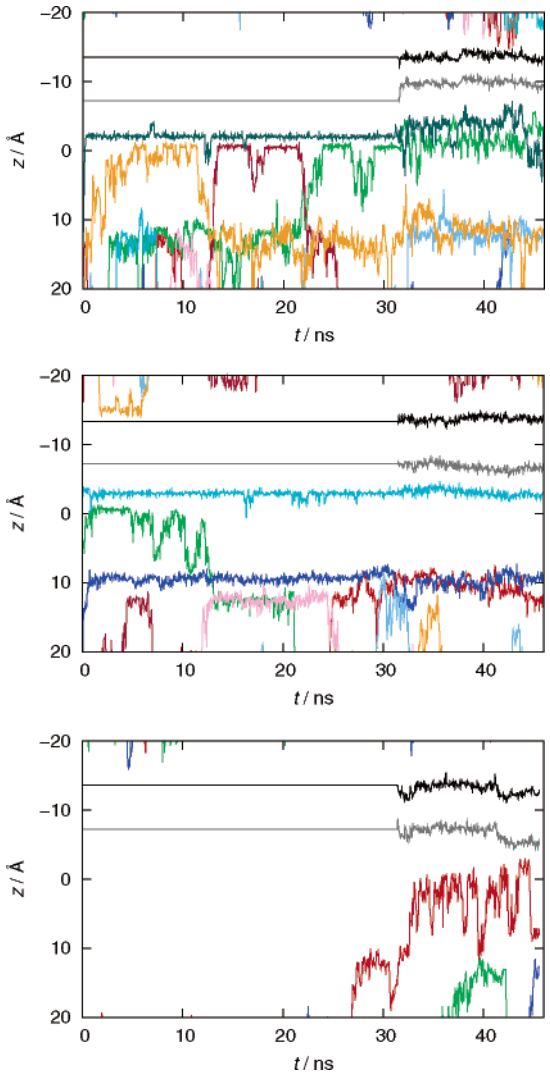

FIGURE 4: *z* coordinates (along the channel axis corresponding to Figure 3) of potassium ions entering and exiting the cavity from the intracellular side (top, KB-KcvWT; middle, KB-KcvΔN8; bottom, KB-KcvP13A).

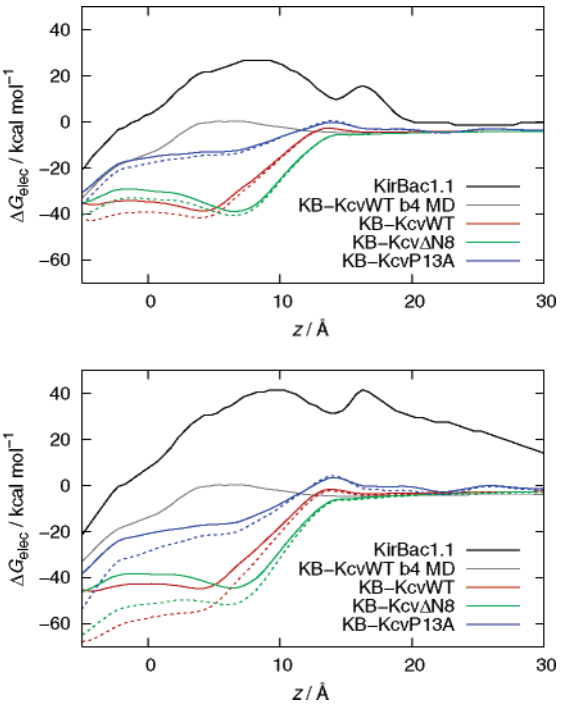

FIGURE 5: Electrostatic transfer free energy profile for K^+ along the channel *z*-axis (red, KB-KcvWT; green, KB-KcvΔN8; blue, KB-KcvP13A; black, original KirBac1.1/PDB code 1P7B; gray, truncated KirBac1.1 corresponding to the initial KB-KcvWT model before simulation). Solid lines: protonated Glu58 (wild type, corresponding to Glu106 in KirBac1.1). Dashed lines: deprotonated Glu58. Top: ionic strength 100 mM. Bottom: ionic strength 0.

comparison to KB-KcvWT. In the Kcv reference system this corresponds to a measurable increase of inward current (*6*). Interestingly, the electrostatic free energy surface of the deletion mutant does not exhibit substantial differences compared to the wild type. Worth noting is that changing the protonation state of Glu58 does not alter the relative trends rendering this position uncritical, neither does increasing the ionic strength from a situation without ionic screening to 100 mM. So from both a sterical and an electrostatic perspective, all three channels produce an open, conductive conformation; however, the P13A mutant results in an even higher conductance state compared to the wild type and deletion mutant. The latter two do not differ much in their sterical and electrostatic properties. It is therefore reasonable to attribute the experimentally measured larger stationary currents in the KcvP13A channel to both sterical and electrostatic factors. The small activity/total inactivity of KcvΔN8/9, on the other hand, must have a different origin.

Salt Bridge Patterns. A remarkable result is found in the context of the structure around the inner mouth which emphasizes the importance of the symmetrizing annealing approach: Figure 6 shows the average configuration of positive residues in the N-terminal slide helix, i.e., Lys9 (WT/P13A) and the terminal methionine, and negative C-terminal Thr94. The C-terminal carboxyl function forms a salt bridge with Lys9 predominantly within the same monomer in the wild-type case and predominantly between neighboring monomers in KB-KcvP13A. For KB-KcvΔN8 no such positively charged partner for the C-terminal threonine is permanently available, giving rise to a change of local permeability of the inner mouth constriction. In the reference system, the totally inactive KcvΔN9, an equivalent positively charged arginine is lost.

These features are not an artifact of the annealing procedure but are also directly reflected by the dynamics, as illustrated with distance time series over the entire rigid filter runs in Figure 7: The data show that a salt bridge is formed if the distance between the amino N and the carboxyl C locks in below 5 Å. Such states are frequently observed for the wild type and P13A mutant between Lys9 and Thr94. The other available positive residue, N-terminal methionine, temporarily locks into a salt bridge configuration with threonine in the cases of P13A and ΔN8 but not so in the case of the wild-type channel. We observe frequent flips between intra- and intermonomer configurations for P13A and also, to a lesser extent, for the wild type. In the deletion mutant the Thr94 carboxyl group is free to find other partners, such as strongly coordinating K^+ ions. Such a configuration blocks the passage of further ions through the constriction. This feature corresponds with the finding that the electrostatic barrier at the constriction is smallest for KB-KcvΔN8 among the variants, indicating local net stabilization for K^+ relative to the other mutants. The presence of GFP

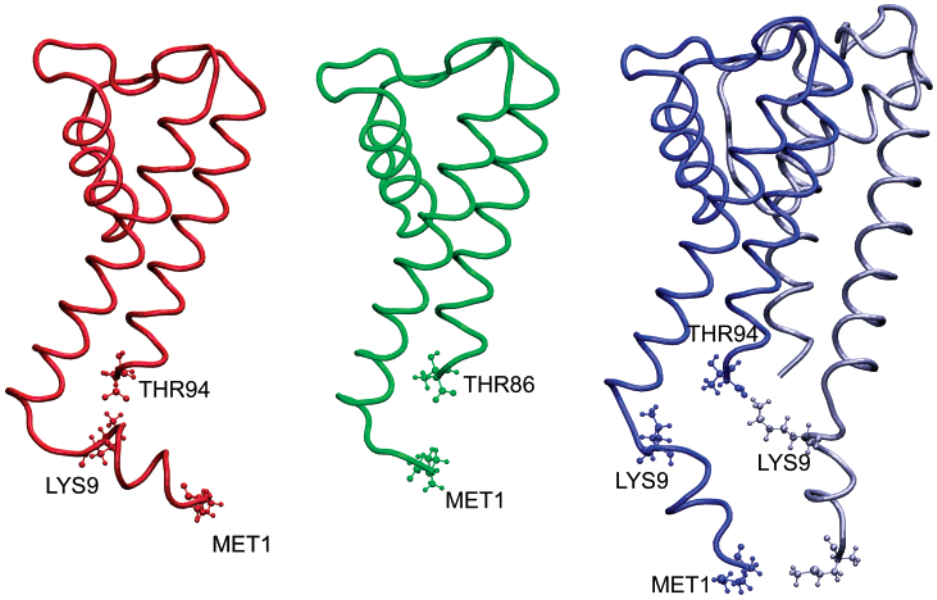

FIGURE 6: Salt bridge patterns observed in symmetrized average structures (red, KB-KcvWT; green, KB-KcvΔN8; blue, KB-KcvP13A).

attached to the C-terminus of channels studied in the corresponding electrophysiological experiments does not disqualify the interpretation suggested here since the linker (sequence EFCSRRYRGPGIHRPVAT) contains a negative group just as the first residue attached to threonine.

The present salt bridges in the vicinity of the inner mouth constriction are not unique to KB-Kcv but have an analogy in the recently resolved X-ray structure of the NaK channel (*42*): structural analysis reveals such motifs between different subunits (Glu23 near the slide helix kink and Arg10 in the N-terminal slide helix) as well as within the same monomer (Glu23 and Lys97 in the C-terminal region). It will certainly be fruitful to study other channels in order to characterize the general role of similar salt bridges in structure−function relationships of ion channels.

The similarity between KB-KcvWT and KB-KcvΔN8 leaves only the change in salt bridge patterns and the resulting potassium block as a reasonable explanation for the apparent inactivity of the Kcv reference system. Apparently, the transport mechanism through the constriction is characterized by a delicate balance between cation coordination and salt bridge flipping. This mechanism is similar for the wild type and point mutant and is disrupted for the deletion mutant due to missing salt bridges. Therefore, the presence of positively charged residues in the N-terminus appears to be a design principle for Kcv-type, and probably other, channels. It is tempting to speculate that the inner constriction resembles a "turnstile" which, together with the cavity, functions as a local buffer device that guarantees an almost constant flux of ions under varying local concentrations near the membrane−cytosol interface.

The similarity of KB-KcvWT and KB-KcvP13A is equally remarkable since it offers the basis for the localization of the presumed inner gate in Kcv-type channels: the higher conductance character of P13A in the open inner-mouth state is adequately explained by sterical and electrostatic factors. Therefore, the different gating kinetics, if they are related to an inner gate, must be caused by the N-terminal sequence up to the kink at Pro13. The N-terminus itself probably represents a gate. We cannot rule out the possibility that the effect of mutations is transmitted to the filter region. However, a simple vibrational coupling mechanism appears to be unlikely (*19*), and we have not found any other dynamical evidence.

Integral Equation Theory. The results from 3D-RISM theory illustrate and summarize the preceding discussions in a compact way. They furthermore elucidate the origin of the apparent potassium blockage found for the deletion mutant. Potassium densities around the fully solvated channel proteins are shown in Figure 8. The extracellular side of the filter is characterized by large high-density regions which correspond to extended funnel-like free energy basins responsible for pulling bulk potassium into the filter region. This motif is, as expected, found for all variants. Integral equation theory is capable of locating the distinct K^+ filter positions as well as the K^+ binding sites between Glu58 and Asp67 in each monomer. Large density is also found within the cavities of the wild type and deletion mutant and, to slightly lesser extent particularly near the mouth, in the P13A variant. All of these data agree quite well with the sterical/electrostatic picture developed above.

RISM theory, in contrast to Poisson−Boltzmann analysis, allows a deeper view into the consequences of missing salt bridges: KB-KcvΔN8 shows a substantial increase of potassium density right behind the constriction on the cytosolic side which has no analogy in the other variants. This free energy basin is the thermodynamic origin of the tight K^+ coordination leading to substantial escape barriers that are not found by purely electrostatic approaches. In contrast to the filter region where large barriers are effectively reduced by concerted single-file motion, such a mechanism appears to be impossible if only a single coordination partner like the C-terminal carboxyl function is present.

The integral equation approach is obviously quite powerful for characterizing the single-ion free energy surface of channels. On the other hand, the results indicate that our simulation time was indeed long enough to sample essential properties of the variants: Most dynamical features detected

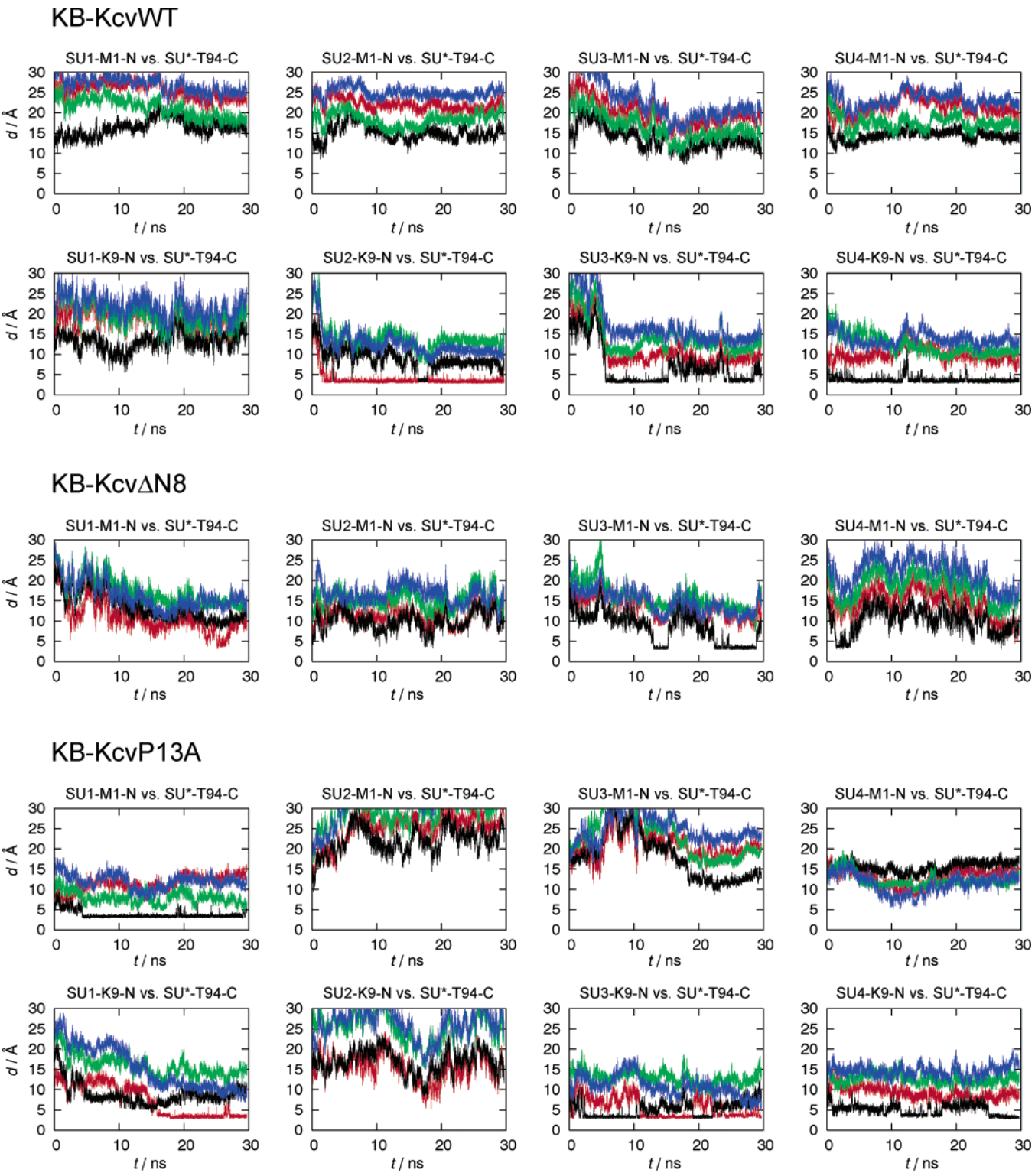

FIGURE 7: Salt bridge constituent time series for distances between the amino N of positive residues and the carboxyl C. The header of each plot encodes the residue index for the respective atoms (example: SU1-K9-N = *SU*bunit*1*, residue *Lys9*, amino *N*itrogen). Every plot shows the evolution for a specific atom versus its counterpart in all four subunits (indicated by the wild card SU*). Key: black, atoms belong to the same monomer; colored, atoms belong to different monomers.

by direct inspection of the trajectories can be related to the density distributions. It will certainly be fruitful to use this technique for further ion channel studies.

DISCUSSION

Based upon the hypothesis of structural and functional analogy between Kcv mutants and our three KirBac1.1 mutant models, our results allow the identification of key features of the channel protein that characterize the role of the N-terminus for channel function:

(a) The effect of mutations is highly localized. Although this may be related to the fixed filter geometry applied in the production simulations, the procedure is justified by the results of the network model analysis by Shrivastava and

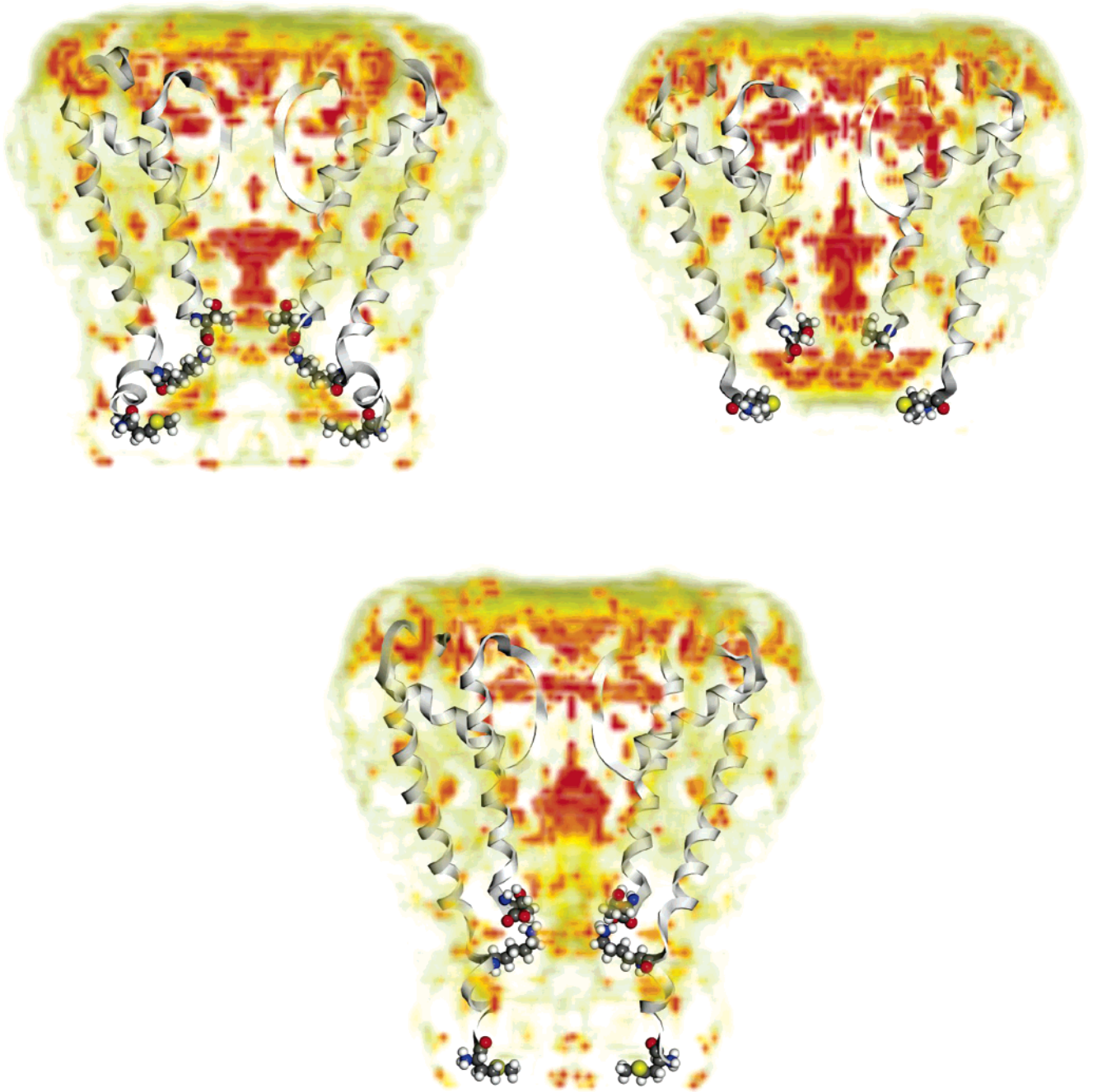

FIGURE 8: Color-coded potassium density distribution from 3D-RISM-KH theory around fully solvated WT and mutant channel structures in 1 M KCl solution (top left, KB-KcvWT; top right, KB-KcvΔN8; bottom, KB-KcvP13A). Density increases from transparent (bulk value and below) over gray and yellow to red. C- and N-terminal amino acids as well as Lys9 are explicitly depicted.

Bahar (*19*) and by inspection of fully relaxed simulations. All observables agree with the assumption that the cytoplasmic side of the channel is open in the present simulations, regardless of the effect of any mutation, as evidenced by spontaneous ion transition events into the cavity from the cytosolic side. Structurally and energetically, the deletion mutant is equally open but appears to be in an inactivated state [see also (c)].

(b) The intracellular mouth is defined by a hydrophilic constriction formed by the C-terminal amino acids, in contrast to other known K^+ channel structures where the inner gate is characterized by a hydrophobic constriction via bundle crossing of transmembrane segments. The carboxyl functions flip frequently between an orientation toward the channel axis when an ion is actually passing the constriction and a salt bridge with positively charged residues in the N-terminus, if available. Similar salt bridge patterns are observed in the recently resolved structure of the NaK channel (*42*). The inner constriction presumably operates like a turnstile guaranteeing an almost constant ion flux in conjunction with the cavity.

(c) The function of the inner constriction, which is not the gate itself (see below), is directly related to the presence of these salt bridges. Deleting positive groups leads to channel inactivation. This is related to a change of the role of carboxyl groups that block the passage of further cations by coordinating tightly with a potassium ion in the absence of a salt bridge partner. Neither sterical nor purely electro-

static factors seem to be responsible for the apparent inactivation. Integral equation theory is capable of characterizing the situation fully. The presence of positively charged residues in the N-terminus appears to be a design principle for potassium channels characterized by short C-termini or by the presence of negative charges at relevant positions.

(d) We did not observe a significant change of the transmembrane domains with respect to their orientation or bending as a result of mutations. The N-terminal slide helices are very flexible and do not exhibit significant contact with the lipid environment.

(e) The localized effect of the N-terminal P13A mutation leads to both sterical and electrostatic factors favoring ion permeability into and out of the cavity. This is compatible with the observation that the analogous mutation causes an increase of steady-state current in Kcv (*20*). From the similarity between the wild type and P13A mutant in the constriction area we can conclude that the inner gate, if it exists, is not directly located at the region of smallest sterical pore diameter. On the other hand, as long as we accept the functional analogy between Kcv and the simulated chimeras, the different time-dependent current component of the P13A mutant can only be understood if the N-terminus itself acts as a cytosolic gate. Alternatively, but unlikely, the effect of mutations could be transmitted to the filter region.

In summary, Kcv possesses, compared to other known potassium channels, very genuine but also a number of certain common structural elements. The role of all these elements for the open pore state was partially understood in the present work. For a complete microscopic dynamical picture of channel function and gating kinetics, however, we need to understand the structure of the closed state, the cytosolic gating mechanism, and its regulation and coupling to the filter gate from an atomic perspective. The "functional analogy" hypothesis needs further examination by cross-checking the results for KB-Kcv with simulations of atomistic Kcv models. Work into this direction is currently in progress.

ACKNOWLEDGMENT

Computer time was provided on IBM Regatta systems at the Hochschulrechenzentrum Darmstadt and at the Forschungszentrum Jülich. We thank J. Brickmann and the MOLCAD GmbH for providing the MOLCAD visualization program.

REFERENCES

1. Plugge, B., Gazzarrini, S., Nelson, M., Cerana, R., Van Etten, J. L., Derst, C., DiFrancesco, D., Moroni, A., and Thiel, G. (2000) A potassium channel protein encoded by chlorella virus PBCV-1, *Science 287*, 1641−1644.
2. Gazzarrini, S., Severino, M., Lombardi, M., Morandi, M., DiFrancesco, D., Van Etten, J. L., Thiel, G., and Moroni, A. (2003) The viral potassium channel Kcv: structural and functional features, *FEBS Lett. 552*, 12−16.
3. Kang, M., Graves, M., Mehmel, M., Moroni, A., Gazzarrini, S., Thiel, G., Gurnon, J. R., and Van Etten, J. L. (2004) Genetic diversity in chlorella viruses flanking Kcv, a gene that encodes a potassium ion channel protein, *Virology 326*, 150−159.
4. Heginbotham, L., Abramson, T., and MacKinnon, R. (1992) A functional connection between the pores of distantly related ion channels as revealed by mutant K^+ channels, *Science 258*, 1152−1155.
5. Kuo, A., Gulbis, J. M., Antcliff, J. F., Rahman, T., Lowe, E. D., Zimmer, J., Cuthbertson, J., Ashcroft, F. M., Ezaki, T., and Doyle, D. A. (2003) Crystal structure of the potassium channel KirBac1.1 in the closed state, *Science 300*, 1922−1926.
6. Gazzarrini, S., Kang, M., Van Etten, J. L., Tayefeh, S., Kast, S. M., DiFrancesco, D., Thiel, G., and Moroni, A. (2004) Long-distance interactions within the potassium channel pore are revealed by molecular diversity of viral proteins, *J. Biol. Chem. 279*, 28443−28449.
7. Doyle, D. A. (2004) Structural changes during ion channel gating, *Trends Neurosci. 27*, 298−302.
8. Doyle, D. A. (2004) Structural themes in ion channels, *Eur. Biophys. J. 33*, 175−179.
9. Perozo, E., Cortes, D. M., and Cuello, L. G. (1999) Structural rearrangements underlying K^+-channel activation gating, *Science 285*, 73−78.
10. Beckstein, O., Biggin, P. C., Bond, P., Bright, J. N., Domene, C., Grottesi, A., Holyoake, J., and Sansom, M. S. P. (2003) Ion channel gating: insights via molecular simulations, *FEBS Lett. 555*, 85−90.
11. Grottesi, A., Domene, C., Hall, B., and Sansom, M. S. P. (2005) Conformational dynamics of M2 helices in KirBac channels: Helix flexibility in relation to gating via molecular dynamics simulations, *Biochemistry 44*, 14586−14594.
12. Kuo, A., Domene, C., Johnson, L. N., Doyle, D. A., and Vénien-Bryan, C. (2005) Two different conformational states of the KirBac3.1 potassium channel revealed by electron crystallography, *Structure 13*, 1463−1472.
13. Robertson, J. L., and Roux, B. (2005) One channel: open and closed, *Structure 13*, 1398−1400.
14. Roux, B. (2005) Ion conduction and selectivity in K^+ channels, *Annu. Rev. Biophys. Biomol. Struct. 34*, 153−171.
15. Bichet, D., Lin, Y., Ibarra, C. A., Huang, C. S., Yi, B. A., Jan, Y. N., and Jan, L. Y. (2004) Evolving potassium channels by means of yeast selection reveals structural elements important for selectivity, *Proc. Natl. Acad. Sci. U.S.A. 101*, 4441−4446.
16. Domene, C., Grottesi, A., and Sansom, M. S. P. (2004) Filter flexibility and distortion in a bacterial inward rectifier K^+ channel: Simulation studies of KirBac1.1, *Biophys. J. 87*, 256−267.
17. VanDongen, A. M. J. (2004) K channel gating by an affinity switching selectivity filter, *Proc. Natl. Acad. Sci. U.S.A. 101*, 3248−3252.
18. Corsero-Morales, J. F., Cuello, L. G., Zhao, Y., Jogini, V., Cortes, D. M., Roux, B., and Perozo, E. (2006) Molecular determinants of gating at the potassium-channel selectivity filter, *Nat. Struct. Mol. Biol. 13*, 311−318.
19. Shrivastava, I. H., and Bahar, I. (2006) Common mechanism of pore opening shared by five different potassium channels, *Biophys. J. 90*, 3929−3940.
20. Hertel, B., Tayefeh, S., Mehmel, M., Kast, S. M., Van Etten, J. L., Moroni, A., and Thiel, G. (2006) Elongation of outer transmembrane domain alters function of miniature K^+ channel Kcv, *J. Membr. Biol. 210*, 1−9.
21. Moroni, A., Viscomi, C., Sangiorgio, V., Pagliuca, C., Meckel, T., Horvath, F., Gazzarrini, S., Valbuzzi, P., Van Etten, J. L., DiFrancesco, D., and Thiel, G. (2002) The short N-terminus is required for functional expression of the virus-encoded miniature K(+) channel Kcv, *FEBS Lett. 530*, 65−69.
22. Hertel, B. (2005) Struktur-Funktions-Beziehung in dem minimalen viralen K^+-Kanal Kcv: Funktionelle Rolle des N-Terminus bei der Regulation von Kanalaktivität, Ph.D. Thesis, Technische Universität Darmstadt, Darmstadt, Germany.
23. Sansom, M. S. P., Shrivastava, I. H., Bright, J. N., Tate, J., Capener, C. E., and Biggin, P. C. (2002) Potassium channels: structures, models, simulations, *Biochim. Biophys. Acta 1565*, 294−307.
24. Woolf, T. B., and Roux, B. (1994) Molecular dynamics simulation of the gramicidin channel in a phospholipid bilayer, *Proc. Natl. Acad. Sci. U.S.A. 91*, 11631−11635.
25. Woolf, T. B., and Roux, B. (1996) Structure, energetics, and dynamics of lipid-protein interactions: A molecular dynamics study of the gramicidin A channel in a DMPC bilayer, *Proteins: Struct., Funct., Genet. 24*, 92−114.
26. Berneche, S., and Roux, B. (2000) Molecular dynamics of the KcsA K(+) channel in a bilayer membrane, *Biophys. J. 78*, 2900−2917.
27. Allen, T. W., Kuyucak, S., and Chung, S. H. (1999) Molecular dynamics study of the KcsA potassium channel, *Biophys. J. 77*, 2502−2516.

28. Roux, B., Allen, T., Bernèche, S., and Im, W. (2004) Theoretical and computational models of biological ion channels, *Q. Rev. Biophys. 37*, 15−103.
29. Capener, C. E., Shrivastava, I. H., Ranatunga, K. M., Forrest, L. R., Smith, G. R., and Sansom, M. S. P. (2000) Homology modeling and molecular dynamic simulation studies of an inward rectifier potassium channel, *Biophys. J. 78*, 2929−2942.
30. Capener, C. E., Kim, H. J., Arinaminpathy, Y., and Sansom, M. S. P. (2002) Ion channels: structural bioinformatics and modelling, *Hum. Mol. Genet. 11*, 2425−2433.
31. Haider, S., Grottesi, A., Hall, B. A., Ashcroft, F. M., and Sansom, M. S. P. (2005) Conformational dynamics of the ligand-binding domain of inward rectifier K channels as revealed by molecular dynamics simulations: toward an understanding of Kir channel gating, *Biophys. J. 88*, 3310−3320.
32. Yu, K., Fu, W., Liu, H., Luo, X., Chen, K. X., Ding, J., Shen, J., and Jiang, H. (2004) Computational simulations of interactions of scorpion toxins with the voltage-gated potassium ion channel, *Biophys. J. 86*, 3542−3555.
33. Roux, B., Berneche, S., and Im, W. (2000) Ion channels, permeation, and electrostatics: insight into the function of KcsA, *Biochemistry 39*, 13295−13306.
34. Beglov, D., and Roux, B. (1997) An integral equation to describe the solvation of polar molecules in liquid water, *J. Phys. Chem. B 101*, 7821−7826.
35. Kovalenko, A., and Hirata, F. (1998) Three-dimensional density profiles of water in contact with a solute of arbitrary shape: a RISM approach, *Chem. Phys. Lett. 290*, 237−244.
36. Cui, Q. Z., and Smith, V. H. (2002) K^+/Na^+ selectivity of KcsA potassium channel analyzed by reference interaction site model (RISM) integral equation theory, *Chem. Phys. Lett. 365*, 110−116.
37. Cui, Q. Z., and Smith, V. H. (2005) Analysis of K^+/Na^+ selectivity of KcsA potassium channel with reference interaction site model theory, *Mol. Phys. 103*, 191−201.
38. Doyle, D. A., Cabral, J. C., Pfuetzner, R. A., Kuo, A., Gulbis, J. M., Cohen, S. L., Chait, B. T., and MacKinnon, R. (1998) The structure of the potassium channel: molecular basis of K^+ conduction and selectivity, *Science 280*, 69−77.
39. Jiang, Y., Lee, A., Chen, J., Cadene, M., Chait, B. T., and MacKinnon, R. (2002) Crystal structure and mechanism of a calcium-gated potassium channel, *Nature 417*, 515−522.
40. Jiang, Y., Lee, A., Chen, J., Ruta, V., Cadene, M., Chait, B. T., and MacKinnon, R. (2003) X-ray structure of a voltage-dependent K^+ channel, *Nature 423*, 33−41.
41. Long, S. B., Campbell, E. B., and MacKinnon, R. (2005) Crystal structure of a mammalian voltage-dependent Shaker family K^+ channel, *Science 309*, 897−903.
42. Shi, N., Sheng, Y., Alam, A., Chen, L., and Jiang, Y. (2006) Atomic structure of a Na^+ and K^+ conducting channel, *Nature 23*, 427−429.
43. Durell, S. R., and Guy, H. R. (1999) Structural models of the KtrB, TrkH, and Trk1,2 symporters based on the structure of the KcsA K^+ channel, *Biophys. J. 77*, 789−807.
44. Brooks, B. R., Bruccoleri, R. E., Olafson, B. D., States, D. J., Swaminathan, S., and Karplus, M. (1983) CHARMM: a program for macromolecular energy, minimization, and dynamics calculations, *J. Comput. Chem. 4*, 187−217.
45. Sali, A., and Blundell, T. L. (1993) Comparative protein modelling by satisfaction of spatial restraints, *J. Mol. Biol. 234*, 779−815.
46. Berneche, S., and Roux, B. (2002) The ionization state and the conformation of Glu-71 in the KcsA K^+ channel, *Biophys. J. 82*, 772−780.
47. Kale, L., Skeel, R., Bhandarkar, M., Brunner, R., Gursoy, A., Krawetz, N., Phillips, J., Shinozaki, A., Varadarajan, K., and Schulten, K. (1999) NAMD2: greater scalability for parallel molecular dynamics, *J. Comput. Phys. 151*, 283−312.
48. MacKerell, A. D., Jr., Bashford, D., Bellott, M., Dunbrack, R. L., Evanseck, J. D., Field, M. J., Fischer, S., Gao, J., Guo, H., Ha, S., Joseph-McCarthy, D., Kuchnir, L., Kuczera, K., Lau, F. T. K., Mattos, C., Michnick, S., Ngo, T., Nguyen, D. T., Prodhom, B., Reiher, W. E., Roux, B., Schlenkrich, M., Smith, J. C., Stote, R., Straub, J., Watanabe, M., Wiorkiewicz-Kuczera, J., Yin, D., and Karplus, M. (1998) All-atom empirical potential for molecular modelling and dynamics studies of proteins, *J. Phys. Chem. B 102*, 3586−3616.
49. Schlenkrich, M., Brickmann, J., MacKerell, A. D., Jr., and Karplus, M. (1996) An empirical potential energy function for phospholipids: criteria for parameter optimization and applications, in *Biological Membranes: A Molecular Perspective from Computation and Experiment* (Merz, K. M., and Roux, B., Eds.) pp 31−81, Birkkäuser, Boston, MA.
50. Jorgensen, W. L., Chandrasekhar, J., and Madura, J. D. (1983) Comparison of simple potential functions for simulating liquid water, *J. Chem. Phys. 79*, 926−935.
51. Roux, B. (2006) http://thallium.bsd.uchicago.edu/RouxLab/.
52. Ryckaert, K. P., Ciccoti, G., and Berendsen, H. J. C. (1977) Numerical integration of the Cartesian equation of motions of a system with constraints: molecular dynamics of *n*-alkanes, *J. Comput. Chem. 23*, 327−341.
53. Essmann, U., Perera, L., Berkowitz, M. L., Darden, T., Lee, H., and Pedersen, L. G. (1995) A smooth particle mesh Ewald method, *J. Chem. Phys. 103*, 8577−8593.
54. Tu, K., Tobias, D. J., and Klein, M. L. (1995) Constant pressure and temperature molecular dynamics simulation of a fully hydrated liquid crystal phase dipalmitoylphosphatidylcholine bilayer, *Biophys. J. 69*, 2558−2562.
55. Feller, S. E., Zhang, Y., Pastor, R. W., and Brooks, B. R. (1995) Constant pressure molecular dynamics simulation: the Langevin piston method, *J. Chem. Phys. 103*, 4613−4621.
56. Bernèche, S., Nina, M., and Roux, B. (1998) Molecular dynamics simulation of melittin in a dimyristoylphosphatidylcholine bilayer membrane, *Biophys. J. 75*, 1603−1618.
57. Smart, O. S., Neduvelil, J. G., Wang, X., Wallace, B. A., and Sansom, M. S. P. (1996) HOLE: a program for the analysis of the pore dimensions of ion channel structural models, *J. Mol. Graphics 14*, 354−360.
58. Honig, B., Sharp, K., and Yang, A. S. (1993) Macroscopic models of aqueous solutions: biological and chemical applications, *J. Phys. Chem. 97*, 1101−1109.
59. Weill Medical College of Cornell University, Department of Physiology and Biophysics (2005) RMSDTT: RMSD Trajectory Tool, http://physiology.med.cornell.edu/faculty/hweinstein/vmd-plugins/rmsdtt/.
60. Humphrey, W., Dalke, A., and Schulten, K. (1996) VMD−visual molecular dynamics, *J. Mol. Graphics 14*, 33−38.
61. Jogini, V., and Roux, B. (2005) Electrostatics of the intracellular vestibule of K^+ channels, *J. Mol. Biol. 354*, 272−288.
62. Nina, M., Beglov, D., and Roux, B. (1997) Atomic radii for continuum electrostatics calculations based on molecular dynamics free energy simulations, *J. Phys. Chem. B 1001*, 5239−5248.
63. Im, W., Beglov, D., and Roux, B. (1998) Continuum solvation model: computation of electrostatic forces from numerical solutions to the Poisson-Boltzmann equation, *Comp. Phys. Commun. 111*, 59−75.
64. Perkyns, J., and Pettitt, B. M. (1992) A site-site theory for finite concentration saline solutions *J. Chem. Phys. 97*, 7656−7666.
65. Kovalenko, A., and Hirata, F. (2000) Potentials of mean force of simple ions in ambient aqueous solution. I. Three-dimensional reference interaction site model approach, *J. Chem. Phys. 112*, 10391−10402.
66. Kovalenko, A., Ten-No, S., and Hirata, F. (1999) Solution of three-dimensional reference interaction site model and hypernetted chain equations for simple point charge water by modified method of direct inversion in iterative subspace, *J. Comput. Chem. 20*, 928−936.
67. Laliberté, M., and Cooper, W. E. (2004) Model for calculating the density of aqueous electrolyte solutions, *J. Chem. Eng. Data 49*, 1141−1151.
68. Hasted, J. B., Ritson, D. M., and Collie, C. H. (1948) Dielectric properties of aqueous ionic solutions. Parts I and II, *J. Chem. Phys. 16*, 1−21.
69. Kovalenko, A., and Hirata, F. (1999) Potential of mean force between two molecular ions in a polar molecular solvent: a study by the three-dimensional reference interaction site model, *J. Phys. Chem. B 103*, 7942−7957.
70. Brickmann, J., Goetze, T., Heiden, W., Moeckel, G., Reiling, S., Vollhardt, H., and Zachmann, C.-D. (1995) Interactive visualization of molecular scenarios with MOLCAD/SYBYL, in *Data Visualisation in Molecular Science: Tools for Insight and Innovation* (Bowie, J. E., Ed.) pp 83−97, Addison-Wesley, Reading, MA.
71. Grottesi, A., Domene, C., Haider, S., and Sansom, M. S. P. (2005) Molecular dynamics simulation approaches to K channels: conformational flexibility and physiological function, *IEEE Trans. Nanobiosci. 4*, 112−119.

72. Shrivastava, I. H., and Sansom, M. S. P. (2000) Simulations of ion permeation through a K channel: molecular dynamics of KcsA in a phosphor-lipid bilayer, *Biophys. J. 78*, 557−570.
73. Domene, C., Vemparala, S., Klein, M. L., Vénien-Bryan, C., and Doyle, D. A. (2006) Role of aromatic localization in the gating process of a potassium channel, *Biophys. J. 90*, L01−L03.
74. Pagliuca, C., Goetze, T. A., Wagner, R., Thiel, G., Moroni, A., and Parcej, D. (2007) Molecular properties of Kcv, a viral-encoded K^+ channel, *Biochemistry 46*, 1079−1090.

BI602468R